Scattering of a plane electromagnetic wave by a generalized Luneburg sphere—Part 2: Wave scattering and time-domain scattering

Philip Laven [a,*], James A. Lock [b], John A. Adam [c]

[a] 9 Russells Crescent, Horley RH6 7DJ, United Kingdom
[b] Physics Dept., Cleveland State University, Cleveland, OH 44115, USA
[c] Dept. of Mathematics and Statistics, Old Dominion University, Norfolk, VA 23529, USA

ABSTRACT

We calculated scattering of an electromagnetic plane wave by a radially inhomogeneous particle and a radially inhomogeneous bubble when the square of the refractive index profile is parabolic as a function of radius. Such a particle or bubble is called a generalized Luneburg lens. A wide variety of scattering phenomena can occur, depending on the value of the two adjustable parameters of the parabola. These phenomena, including transmission rainbows, the weak caustic for near-critical-angle scattering by a bubble, surface orbiting, the interior orbiting paths of morphology-dependent resonances, and the separation of diffraction are studied here using wave theory and time domain scattering. These phenomena are also compared with their appearance or absence for scattering by a homogeneous sphere.

© 2015 Elsevier Ltd. All rights reserved.

1. Introduction

This paper is a continuation of [1] in which we analyzed transmission scattering by a generalized Luneburg lens (GLL) using ray theory. We here examine the most interesting features of the ray theory analysis using wave theory for plane wave incidence and time domain scattering of an incident femtosecond pulse, which produces the scattered intensity as a function of both angle and delay time. As was mentioned in [1] we consider the refractive index profile of a GLL solely because every scattering quantity is exactly soluble in ray theory. The results described here and in [1] are not particular to a GLL, but are expected to be valid to a large degree for a wide variety of generically similar refractive index profiles.

The body of this paper is organized as follows. In Section 2, we briefly recall the GLL geometry. In Section 3, we numerically compute the transverse electric (TE) and transverse magnetic (TM) scattered intensity for a finely-stratified multi-layer sphere that approximates the refractive index profile of the GLL, using the parallel iteration method. In Section 4 we compute time domain scattering by calculating the scattered fields of Section 3 for each plane wave component in the Fourier spectrum of an incident femtosecond beam and then adding the results together. Lastly, in Section 5 we make a few final comments concerning our more unusual, significant, and interesting results.

2. Geometry of a generalized Luneburg lens

As was the case in [1], we consider an electromagnetic plane wave of amplitude E_0, wavelength λ, wave number $k=2\pi/\lambda$, linearly polarized in the x direction, and propagating in the $+z$ direction in an external medium of refractive

index 1. The plane wave is scattered by a GLL of radius a whose center is at the origin of coordinates, and has the radially inhomogeneous refractive index profile

$$N(r) = \left[2B - C(r/a)^2\right]^{1/2}, \qquad (1)$$

where B and C are positive or negative constants. For easy reference in this paper, the (B, C) parameter space of Eq. (1), previously given as Fig. 1 of [1], is reproduced here as Fig. 1 as well.

The GLL is particle-like (i.e. $N(r) \geq 1$) in regions η and ψ and on line $\gamma\alpha\beta$, and it is bubble-like (i.e. $N(r) \leq 1$) in regions ν, ξ, σ and on line $\delta\varepsilon\zeta$. When $N(a) > 1$ or $N(a) < 1$ the particle or bubble is said to have a hard edge, and when $N(a) = 1$ it is said to be edgeless. The line segment $0 < B < 1/2$, $C = 0$ describes a homogeneous bubble and the line segment $B > 1/2$, $C = 0$ describes a homogeneous particle. The regions ρ_1, ρ_2, and ρ_3 in Fig. 1 have $N(r) > 1$ for some radii inside the sphere and $N(r) < 1$ for other radii. These cases of mixed character will not be considered here. Similarly, a GLL in region μ, for which $N(a)$ is imaginary will also not be considered.

For the remainder of this paper we label the various scattering process according to the notation for the Debye series decomposition of the partial wave scattering amplitudes for a homogeneous spherical particle [2]. The combination of diffraction and external reflection is denoted by $p = 0$, direct transmission is $p = 1$, and transmission following $p - 1$ internal reflections is $p \geq 2$. In [1] it was found that the GLL can have two $p = 1$ rainbows (hereafter called bows) in portions of regions η and ν, while it has one $p = 1$ bow on line segments γ, δ and in portions of regions ν and ψ. Elsewhere in Fig. 1 there are no $p = 1$ bows.

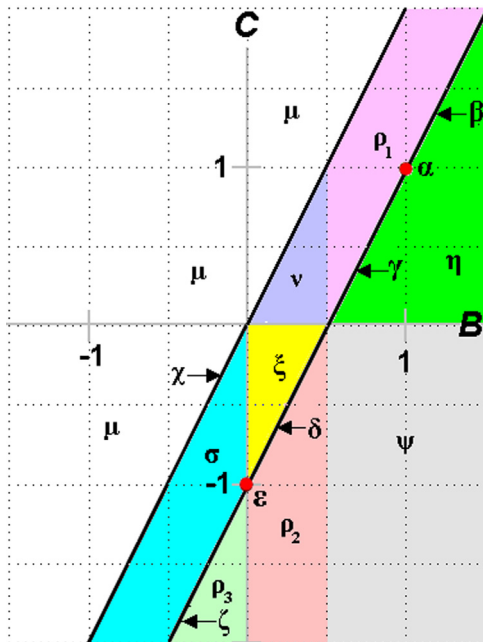**Fig. 1.** (B, C) parameter space.

3. Wave scattering

The ray theory intensity of Sections 3.2 and 4.2 of [1] provides an underlying framework upon which the smoothing and interference effects of wave scattering occur. In this section we consider only those situations for which wave scattering effects significantly depart from their ray scattering counterparts after they have been augmented by diffraction in the near-forward direction. Scattering of a plane wave by a GLL was numerically computed using the parallel iteration approach for a finely-stratified multi-layer sphere. This numerical approach was described fully in [3,4]. The Luneburg sphere was modeled by 128 concentric homogeneous layers of identical thickness, with the refractive index profile discretized to its value at the midpoint of each of the layers. No change in the results was observed when the GLL was decomposed into 256 or more layers. In those situations when the GLLs were edgeless in ray theory, the only scattering processes that occur are diffraction and transmission. However, the multi-layer model will not be truly edgeless due to the discretization process. This will result in a very small amount of spurious $p \geq 2$ scattering admixed into the scattered intensity, which in some cases served as a low-level nuisance background. In the parallel iteration approach the four fundamental scattering amplitudes of [3] were computed for each layer, and then adjacent pairs of amplitudes were combined to produce half as many sets of composite amplitudes of the pairs. This process was repeated, resulting each time in half as many sets of composite amplitudes as in the previous iteration, until only a single set of amplitudes for the entire sphere remained after the final iteration. It is presumed that this approach is less prone to round-off error (because of the fewer number of iterations required), than in the progressive iteration approach [5] where, starting with the innermost layer, one layer at a time is added and the composite amplitudes are updated, until the outermost layer of the sphere is reached.

Numerical computations were performed for an incident wavelength of $\lambda = 0.65$ μm and an overall sphere radius of $a = 100$ μm (except where explicitly noted in the Figures), giving a size parameter of $x = 2\pi a/\lambda = 966.6$, which is sufficiently large so that the underlying ray scattering structure of the intensity should be apparent. The scattering angle is denoted by Θ, and the corresponding angle of incidence in ray theory is denoted by θ_i. For an edgeless particle-like GLL represented by a point on line segment γ of Fig. 1, a bow is predicted in ray theory to occur when $B = 0.75$, $C = 0.5$ at $\Theta_1^R = 30°$.

The TE-polarized wave scattered intensity for this case is shown in Fig. 2. Diffraction dominates for $0° \leq \Theta \leq 3°$ and the transmission bow prominently appears with its principal maximum at $\Theta \approx 28.7°$. This is in reasonable agreement with the expected Airy shifted rainbow scattering angle [6] of $\Theta_1^R = 28.57°$.

Fig. 2 also shows the TE scattered intensity for the hard edge particle-like GLL with $B = 0.76$, $C = 0.5$ in region η of Fig. 1 near line segment γ. As was mentioned in Section 3 of [1], two transmission bows are predicted to occur in ray theory at $\Theta \approx 25.36°$ and $\Theta \approx 31.43°$. However, only the broad relative maximum bow of Fig. 3 of [1] is visible at
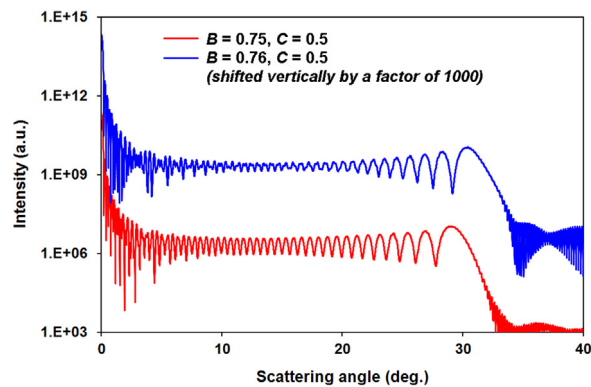
Fig. 2. Wave theory calculations for GLLs of radius $a=100\ \mu m$ for the specified values of B and C on line segment γ and in region η of Fig. 1.

Fig. 3. Wave theory calculations for GLLs of radius $a=100\ \mu m$ for the specified values of B and C on line segment δ and in region ξ of Fig. 1.

$\Theta \approx 30.5°$, while the narrow relative minimum bow at the lower scattering angle is not. The somewhat jagged structure deep in the supernumerary region of Fig. 2 is likely due to $p=3$ scattering. If it had been due to the second transmission bow, the interference would only have occurred between the two bows, and not for $\Theta < 25°$, which is the case in the Figure. We believe the absence of the second transmission bow in wave theory for this size parameter is due to the extreme narrowness of the impact parameter interval responsible for it. Evidence that this is the case is provided by the fact that the finely-stratified multi-layer sphere model was easily able to reproduce both transmission bows for certain other carefully constructed monotonically decreasing refractive index profiles when ray theory predicted that two should occur. Yet other monotonically decreasing refractive index profiles that contain the near-onset of orbiting were found that predicted four transmission bows in ray theory. The details of these calculations will be reported separately.

A transmission bow was also predicted in ray theory for edgeless bubble-like GLLs represented by points on line segment δ of Fig. 1, and two transmission bows were predicted for hard edge bubble-like GLLs in region ξ near line segment δ. The wave theory TE scattered intensity in these two situations for $B=0.25$, $C=-0.5$ and $B=0.24$, $C=-0.5$, respectively, is shown in Fig. 3. Again, the broad relative minimum bow of Fig. 7 of [1] prominently appears in both cases, while for the hard edge Luneburg sphere the relative maximum bow having the smaller deflection angle is absent due to the narrowness of the partial wave interval responsible for it.

As was mentioned in Section 4a of [1], when a ray with $\theta_i > \theta_i^C$, where θ_i^C is the critical angle for total external reflection, is incident on a hard edge bubble-like GLL represented by a point in region ξ of Fig. 1, no light is transmitted into the sphere in ray theory. For $B=0.125$, $C=-0.25$ the critical scattering angle is $\Theta^C=90°$ corresponding to $\theta_i^C=45°$. Partially transmitted rays contribute to the scattered intensity for $0° \leq \Theta \leq \Theta^C$, and their contribution is smoothly extended to $\Theta^C \leq \Theta \leq 180°$ by rapidly damped transmitted electromagnetic surface waves [7–10]. On the other hand, the transition from partial external reflection for $\Theta^C \leq \Theta \leq 180°$ to total external reflection for $0° \leq \Theta \leq \Theta^C$ is continuous in ray theory, but
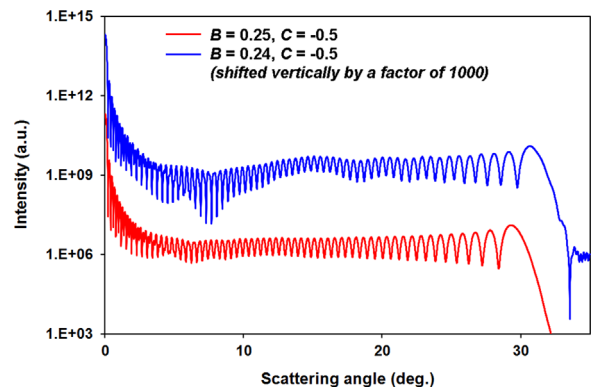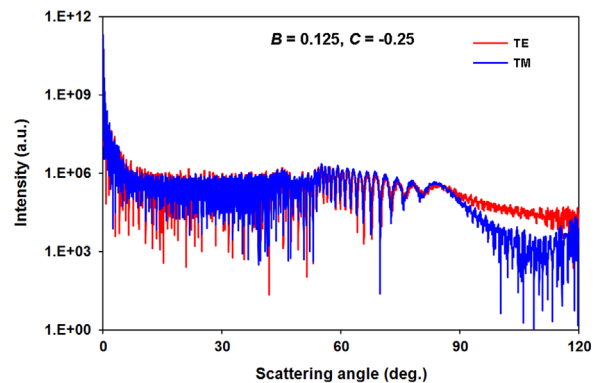

Fig. 4. Wave theory calculations for a GLL of radius $a=100\ \mu m$ with $B=0.125$ and $C=-0.25$ in region ξ of Fig. 1.

it has an infinite slope at the critical angle due to the behavior of the Fresnel reflection coefficient there. This results in what has been termed a weak caustic [10]. The total scattered intensity in the vicinity of Θ^C qualitatively resembles that of a Fresnel straight edge diffraction pattern [11–13] exhibiting the interference between partial transmission and the total external reflection portion of the weak caustic for $0° \leq \Theta \leq \Theta^C$. For $\Theta^C \leq \Theta \leq 180°$ the intensity is dominated by partial external reflection, as at first the transmission surface waves, and then the damped external reflection portion of the weak caustic, decrease in importance. This behavior for $B=0.125$, $C=-0.25$ in region ξ is evident for both the TE and TM polarizations in Fig. 4. It strongly resembles the effect's appearance for scattering by a homogeneous air bubble in water [13].

A weak caustic for transmission, rather than for external reflection, occurs for scattering by the original Luneburg lens with $B=1$, $C=1$ represented by point α in Fig. 1. In this case the infinite discontinuity of the slope of the ray theory electric field at $\Theta^C=90°$ is due to the $[\cos(\Theta_1)]^{1/2}$ dependence of the transmitted field arising from Eq. (23) of [1], rather than from the Fresnel transmission coefficient, which is unity for this edgeless particle-like sphere. The graph of the scattered intensity for this case is shown in Fig. 5. A similar result was obtained using the
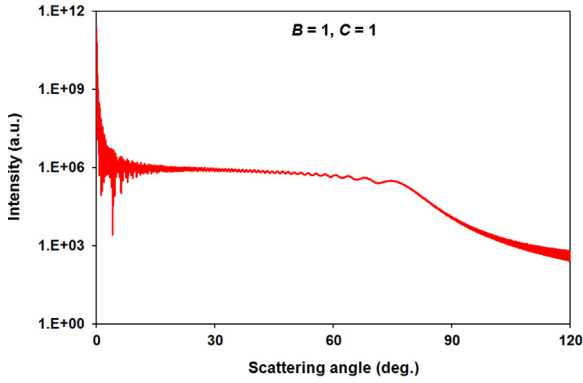
Fig. 5. Wave theory calculations for a GLL of radius $a=100$ μm with $B=1$ and $C=1$ at point α of Fig. 1.

Fig. 6. Wave theory calculations for a GLL of radius $a=100$ μm with $B=0$ and $C=-1$ at point ε of Fig. 1.

progressive iteration method for a multi-layer sphere approximation to a Luneburg lens of size parameter $x=60$ in [14]. Rays with grazing incidence orbit the surface of the Luneburg lens at $r=a$, continually shedding electromagnetic radiation to the far-zone and damping out at a much slower rate than is the case for electromagnetic surface waves [6]. This orbiting radiation dominates over the contribution of the transmission weak caustic for $\Theta^C \le \Theta \le 180°$ producing the slow falloff of the scattered intensity. Shed radiation from both clockwise orbiting rays beginning at the top of the sphere and counterclockwise orbiting rays beginning at the bottom of the sphere produce the fine interference oscillations in this region, and the radiation shed in all azimuthal scattering planes constructively interferes to produce a glory enhancement at $\Theta \approx 180°$. For $0° \le \Theta \le \Theta^C$ the scattered intensity is dominated by the interference between the transmission weak caustic, radiation shed by the orbiting rays, and large angle diffraction [15].

An opportunity to observe a weak caustic unobscured by its interference with other scattering mechanisms is afforded by the edgeless bubble-like GLL having $B=0$, $C=-1$, represented by point ε of Fig. 1. Again the transmitted field in ray theory is $[\cos(\Theta_1)]^{1/2}$ arising from Eq. (23) of [1], and the critical scattering angle is $\Theta_1^C = 90°$. However, for the original Luneburg lens, the on-axis incident ray was transmitted at $\Theta_1 = 0°$, and the transmitted angle increased with increasing impact parameter until $\Theta_1 = 90°$ for the grazing ray (see Fig. 1a of [6]). This grazing ray contribution evolved into the transmission weak caustic along with the more dominant orbiting ray in wave theory. But now it is the on-axis incident ray that is transmitted at $\Theta_1 = -90°$ and evolves into the transmission weak caustic in wave theory. The magnitude of the transmission deflection angle decreases with increasing impact parameter until grazing incident ray has $\Theta_1 = 0°$ (see Fig. 6 of [1]). The resulting TE scattered intensity is given in Fig. 6, and exhibits the weak caustic without competition from stronger overlapping scattering processes.

Morphology-dependent resonances (MDRs) of a GLL occur on line segment β and in the upper portion of region ν where $B < C$. The conditions for the occurrence of an MDR on line segment β were described in [3,16]. However
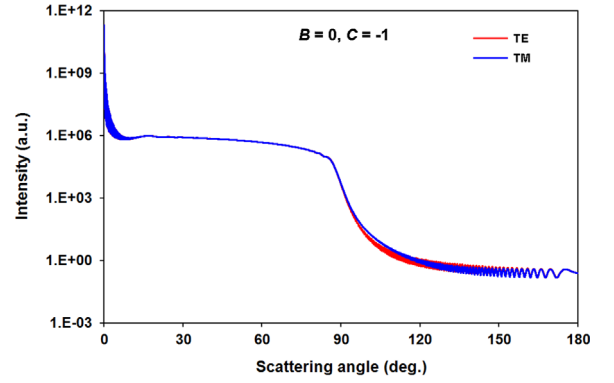
the unusual features of the ray paths of those MDRs have not been previously discussed. By way of introduction to these features, an MDR of a homogeneous spherical particle in wave theory is a radial standing wave of electric field strength localized just inside the sphere's surface. However, a more intuitive, though less quantitatively precise picture can be constructed in ray theory as follows [17]. A ray with the impact parameter $b > a$ just misses striking the sphere. As it passes by, part of its amplitude tunnels through the centrifugal barrier surrounding the sphere until it gets to the surface where it is transmitted to the interior past the critical angle for total internal reflection. The angle of transmission into the sphere with respect to the normal, Φ_1, is obtained by applying Bouguer's law [18] to the ray path at the radius b where the evanescent propagation begins and at the radius r_1 inside the sphere where the propagation switches back from being evanescent to oscillatory. One obtains

$$b = r_1 N(r_1) \sin(\Phi_1). \qquad (2)$$

For a homogeneous sphere where $r_1 = a$, Eq. (2) becomes identical to the extrapolation of Snell's law

$$\sin(\theta_i) = b/a = N \sin(\Phi_a), \qquad (3)$$

where $\sin(\theta_i) > 1$ for rays that classically pass the sphere by. The interior ray then proceeds to cycle around the sphere just beneath the surface, repeatedly undergoing total internal reflection each time the cycling ray strikes the surface. At each strike a small amount of amplitude leaks back out through the centrifugal barrier to the far-zone. A resonant enhancement occurs in ray theory when the optical path length of the interior ray is an integer number of wavelengths per cycle, giving constructive interference between successive cycles. In addition, there is an infinite series of progressively smaller wave theory corrections to this ray prediction [19]. From this heuristic picture, one can see that an MDR of a homogeneous sphere does not occur in any individual Debye series term. Rather, it results from the constructive interference of a very large number of Debye series terms when they are added together.

In contrast, the only Debye series terms contributing to scattering by an edgeless GLL on line segment β are $p=1$ direct transmission, and the diffraction portion of $p=0$. The MDRs of a GLL on line segment β thus occur only in the
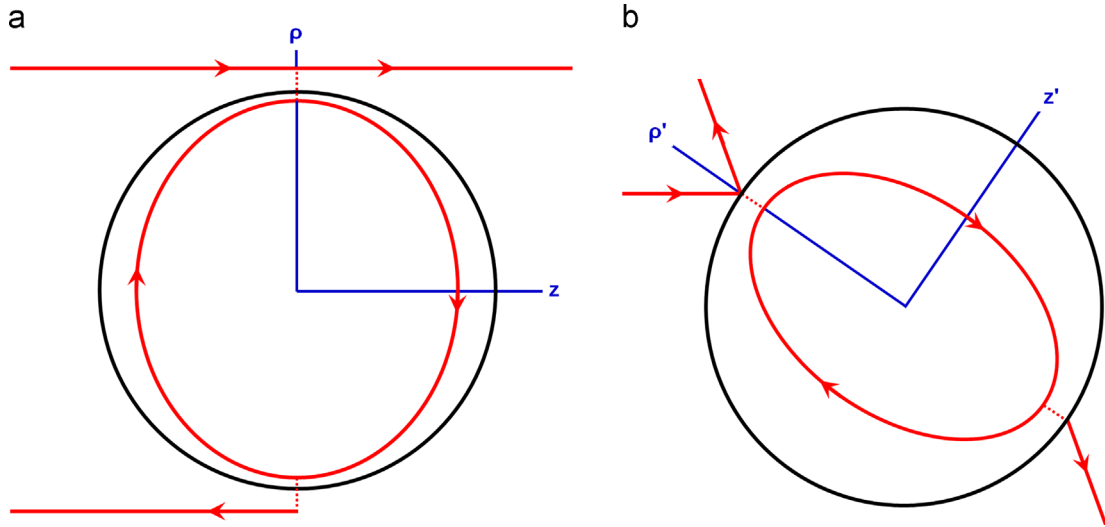
a

b

Fig. 7. Ray path of an MDR for (a) an edgeless particle-like GLL on line segment β, and (b) a hard-edge bubble-like GLL in the upper portion of region ν. The resonance occurs entirely in the $p=1$ term of the Debye series.

$p=1$ Debye series term. How can this happen, given what one knows about the MDRs of a homogeneous sphere? The answer lies in the details of the ray's elliptical path inside a Luneburg sphere when $b > a$. For a GLL on line segment β with $b > a$, the entire elliptical path whose semi-major axis is

$$r_1/a = \left\{ C+1+\left[(C+1)^2-4C\left(b^2/a^2\right)\right]^{1/2} \right\}/2C \qquad (4)$$

and semi-minor axis is

$$r_2/a = \left\{ C+1-\left[(C+1)^2-4C\left(b^2/a^2\right)\right]^{1/2} \right\}/2C \qquad (5)$$

lies inside the sphere, with r_1 along the ρ axis and r_2 along the z axis as defined in [1]. This is illustrated in Fig. 7a.

As was the case for a homogeneous sphere, part of the amplitude of a passing ray with $b > a$ tunnels along the ρ axis through the centrifugal barrier surrounding the sphere until it gets to r_1 inside the sphere, where it is converted to an oscillatory ray with $\Phi_1=90°$, consistent with Eq. (2). Since $r_1 < a$ in this case, Eq. (2) is not identical to Snell's law. The interior ray then repeatedly cycles around on the elliptical ray path, producing a quasi-bound state of light inside the sphere. Each time the cycling ray crosses the $\pm \rho$ axes at r_1, part of the amplitude tunnels back out along the $\pm \rho$ axis giving a contribution to the scattered light in the vicinity of $\Theta=0°$ and $\Theta=180°$, whereas an MDR of a homogeneous sphere emits radiation in all directions. This emission of scattered radiation gives a finite lifetime to the quasi-bound state. In the ray theory picture, an MDR should occur when contributions at these angles from successive interior cycles are in phase with each other. In [3] it was seen that the quality factor of these resonances was relatively low, thus producing a relatively leaky but highly directional source of scattered radiation. Since the ray in question is transmitted into and out of the Luneburg sphere with no intermediate internal reflections at the sphere

surface, the entire MDR is contained in the $p=1$ term of the Debye series, thus resolving the paradox posed above.

The ray theory explanation of MDRs in the upper portion of region ν for a hard-edge bubble-like GLL is similar. When a ray is incident on the sphere past the critical angle for total external reflection $\theta_i > \theta_i^C$ as in Fig. 7b, the path of an interior ray is again an ellipse lying entirely inside the GLL having semi-major axis

$$r_1/a = \left\{ B+\left[B^2-C\,\sin^2(\theta_i)\right]^{1/2} \right\}/C \qquad (6)$$

and semi-minor axis

$$r_2/a = \left\{ B-\left[B^2-C\,\sin^2(\theta_i)\right]^{1/2} \right\}/C. \qquad (7)$$

The semi-major axis coincides with the ρ' axis, which is rotated with respect to the ρ axis of [1] by θ_i, and the semi-minor axis coincides with the z' axis. Part of the amplitude of a ray striking the surface of the bubble-like GLL with $\theta_i > \theta_i^C$ tunnels along the ρ' axis through the classically forbidden portion of the sphere until it gets to the interior point r_1 where it is converted to an oscillatory ray that repeatedly cycles around on the interior elliptical ray path, again producing a quasi-bound state of light inside the sphere. In analogy to the phenomenon of frustrated total internal reflection that occurs when the interfaces are flat [20], the phenomenon described here can be termed frustrated total external reflection. A similar effect, but obtained when a sphere is coated with a material having imaginary refractive index, was proposed in [21]. Each time the interior ray crosses the $\pm \rho'$ axes, part of the amplitude tunnels back out along the $\pm \rho'$ axis giving a contribution to the scattered light in the vicinity of $\Theta=2\theta_i$ and $\Theta=2\theta_i-180°$, again giving a finite lifetime to the quasi-bound state. This MDR also occurs solely in the $p=1$ term of the Debye series. Finally, one should recall that in wave theory, as was the case for a homogeneous

sphere, the MDRs of a Luneburg sphere are a radial standing wave just inside the sphere surface.

The optical path length of the interior ellipse in both the upper portion of region ν and on line segment β is found to be

$$S = 2\pi a B / \left(C^{1/2}\right). \tag{8}$$

Since Eq. (8) is independent of $\sin(\theta_i)$, a purely ray picture of the MDR, without any wave theory input, is unable to predict the resonant size parameter $ka_{resonant}$ of a particular partial wave n when the localization principle [22]

$$\sin(\theta_i) \approx [n(n+1)]^{1/2}/ka \approx (n+\frac{1}{2})/ka \tag{9}$$

is made. Instead, one uses the wave theory argument of [16], namely in the mechanical analogy of scattering by a sphere [23], the effective potential

$$V(r) = 1 - N^2(r) + n(n+1)/(kr)^2 \tag{10}$$

is nearly parabolic as a function of r inside the GLL in the MDR region, thus permitting oscillatory waves inside the parabola. This nearly parabolic effective potential supports a spectrum of approximately harmonic oscillator bound states [24] parameterized by the integer $s=0, 1, 2, …,$. As was discussed in [16], an approximation to the resonant size parameter of an MDR is given when the energy of one of these harmonic oscillator bound states is equal to the effective energy of an incoming partial wave. For the GLL refractive index of Eq. (1), this occurs when

$$ka_{resonant} \approx (2s+n+3/2)(C^{1/2})/B, \tag{11}$$

or

$$2\pi a_{resonant} B / \left(C^{1/2}\right) \approx (2s+n+1+\tfrac{1}{2})\lambda. \tag{12}$$

Since the left hand side of Eq. (12) is the optical length of one cycle of the interior elliptical path of Eq. (8), the extra factor of $\lambda/2$ on the right hand side of Eq. (12) is a wave theory correction arising from the harmonic oscillator zero-point energy to the ray theory integer-number-of-wavelengths prediction, given by $(2s+n+1)\lambda$. The physical origin of the wave correction is at present not known.

The approximation of Eq. (11) with $s=0$ was found in [3] to be quite accurate when applied to the MDRs of a GLL on line segment β. Two possible corrections to Eq. (12) arise from the fact that (i) the effective potential inside the GLL is not exactly parabolic, and (ii) the effective potential extends only out to r_1, and not all the way out to infinity. We tested possibility (i) by Taylor series expanding the potential about its minimum, keeping the quadratic and cubic terms, and then calculating the anharmonic oscillator correction to the bound state energies on line segment β using second order perturbation theory, as is standardly done in quantum mechanics [25]. The correction turned out to be an order of magnitude too small, and was in the correct direction for some resonances but was in the opposite direction for others. We thus feel possibility (ii) holds more promise for improving the theoretical estimate of Eq. (12). Resonances were also examined for $B=0.495$, $C=0.7$ in the upper portion of region ν in the interval $60 \le ka \le 80$. A sequence of eleven nearly evenly-spaced, but distorted, resonance profiles having a relatively low quality factor was found in the interval. Their spacing was $\Delta ka_{resonant} \approx 1.93$, whereas Eq. (12) with $s=0$ predicts $\Delta ka_{resonant}=1.69$. The theoretical prediction is the correct order of magnitude, which is about all that can be expected given the distorted shape of the computed resonance profiles. The reason for the distortion is not known, but it may possibly be due to the simultaneous presence of a sequence of broader $s=1$ resonances, as was the case in [3].

As a final note, in Section 4 of [1], it was mentioned that on line segment ζ and in region σ of Fig. 1, the refractive index changes from real to imaginary inside the GLL at the transition T, causing the forward propagating interior wave to change from being oscillatory to evanescent. In order to adapt this situation to wave theory, the four fundamental scattering amplitudes of the progressive iteration approach must be written at the transition layer in terms of modified Riccati–Bessel functions rather than in terms of the usual Riccati–Bessel functions. This has not been implemented as of yet, and remains a topic for future research.

4. Time domain scattering

It is frequently of interest to assess the contribution of an individual scattering process in situations where many scattering processes occur simultaneously. This is handled naturally in ray theory [26], but in wave theory it is more difficult to accomplish because of the nature of the Mie sum over partial wave scattering amplitudes. There are two approaches to the separation problem in wave theory. First, one can expand the partial wave scattering amplitudes in terms of the Debye series and then examine each Debye term individually [2,7,8]. Second, one can perform a time domain analysis of the total fields scattered in each direction when a short pulse is incident on the sphere. Light waves taking relatively short paths through the particle exit the sphere earlier and are typically due to certain physical processes, while those taking relatively long paths exit the sphere later and are typically due to other processes. This procedure effectively performs a Debye series decomposition of the total wave theory scattered intensity by reading the interference structure between two or more different p-value processes occurring at the same scattering angle, without having to explicitly evaluate the various Debye terms.

A Gaussian plane wave pulse

$$\mathbf{E}^{pulse}(z,t) = E_0 \exp\left[-(z-ct)^2/\sigma^2\right] \exp\left[ik_0(z-ct)\right]\mathbf{u_x} \tag{13}$$

with dominant wavelength $\lambda_0=0.65$ μm, electric field $1/e$ full-width 5 fs and $\sigma=0.75$ μm was Fourier decomposed into its component plane waves. Electromagnetic scattering from each component was computed using the parallel iteration approach for a finely-stratified multi-layer sphere. The scattered fields, weighted by their Fourier amplitude, were then added together to produce the total scattered wave as a function of time. The scattered intensity of the resulting time domain graphs was plotted in false color as a function of the delay time and scattering angle. This procedure is described in more detail in [9,15,27].

Fig. 8a and b shows time domain graphs for the edgeless particle-like GLL with $B=0.75$, $C=0.5$ on line segment γ in Fig. 1 and the edgeless bubble-like GLL with $B=0.25$, $C=-0.5$ on line segment δ, respectively. The inverted-V structure at the top of the graphs centered at $(\Delta t, \Theta)=$ (665 fs, 0°) is the signature of diffraction [15]. The much larger skewed V-like structure beneath it is the signature of transmission. The ray theory prediction of Eqs. (9–12, 28, 29) of [1] is overlaid on the graph, and the impact parameter is denoted for a number of incident rays. In Fig. 8a the cusp point of the large V-like structure is skewed to the right, illustrating the relative maximum of both the scattering angle and the delay time at the particle-like transmission bow. Similarly in Fig. 8b the cusp point of the large V-like structure is skewed to the left, illustrating the relative minimum of both the scattering angle and the delay time for the bubble-like transmission bow. Time domain graphs for $B=0.76$, $C=0.5$ in region η of Fig. 1 and for $B=0.24$, $C=-0.5$ in region ξ where two transmission bows are predicted in ray theory were computed but are not shown here. They were found to be virtually identical to Fig. 8a, and b. In particular, the location of the second bow in the time domain graphs lies directly underneath the dominant $p=1$ trajectory, and is thus not evident in time domain scattering. Had it been offset from the dominant trajectory, as is the case for certain other refractive index profiles which will be reported separately, the second transmission bow would have made its presence known unambiguously.

Fig. 9 illustrates time domain scattering by the hard edge bubble-like GLL with $B=0.125$, $C=-0.25$ in region ξ of Fig. 1. The contributions of the various Debye scattering processes are labeled for $0 \leq p \leq 4$. The inverted-V signature of diffraction is centered at (500 fs, 0°), and the $p=0$ external reflection signature merges smoothly onto its smaller time-delay arm. The location of the on-axis ray for $p=1, 2, 3$ is (385 fs, 0°), (770 fs, 180°), and (1155 fs, 0°) respectively. All these time domain trajectories merge at the total external reflection accumulation point [10] located at (195 fs, 90°). A qualitatively similar time domain graph for scattering by an air bubble in water is illustrated in [28].

In Section 3 of [1] the slow falloff of the scattered intensity for $\Theta > 90°$ for the original Luneburg lens with $B=1$, $C=1$ represented by point α in Fig. 1 was attributed to radiation shed by the ray with grazing incidence as it was captured by the Luneburg lens and proceeded to orbit around the sphere at its surface. This orbiting interpretation is supported by the time domain scattering plot of Fig. 10 where the $p=1$ scattering signature continues for more than a full cycle of orbiting, containing the points (181 fs, 180°) for a half cycle, (276 fs, 0°) for a full cycle, and (381 fs, 180°) for 1.5 cycles.

Some years ago a large monetary prize was informally and semi-jokingly offered for a demonstration of how diffraction could be fully separated off from all the other Debye series scattering processes [29]. It had been demonstrated long ago [7] that such a separation is
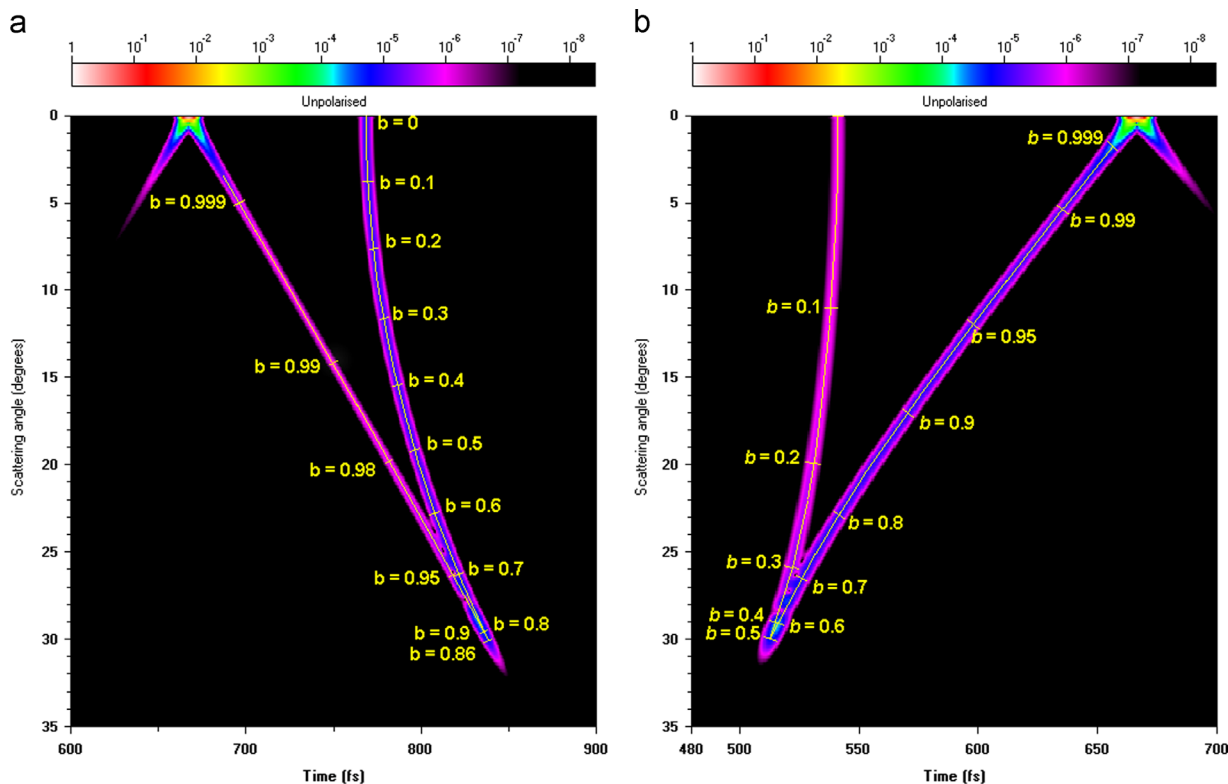

Fig. 8. Time domain diagram for GLLs of radius $a=100$ μm with (a) $B=0.75$, $C=0.5$ on line segment γ and (b) $B=0.25$, $C=-0.5$ on line segment δ of Fig. 1.
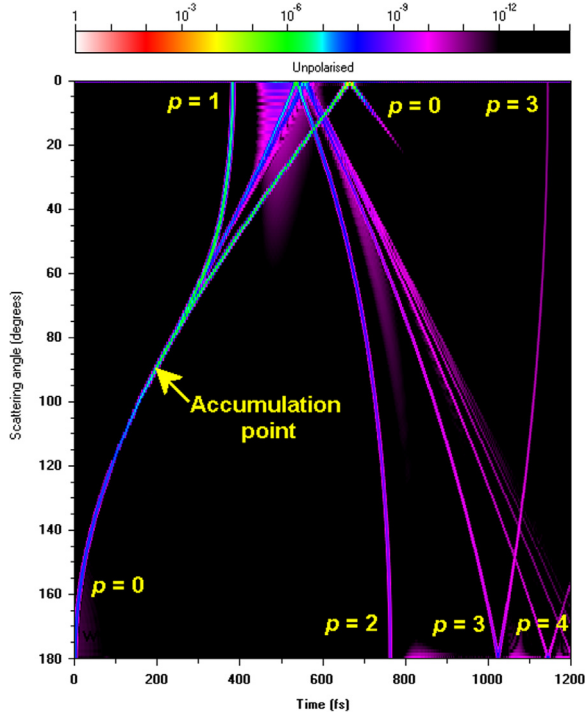
Fig. 9. Time domain diagram for a GLL of radius $a=100\,\mu m$ with $B=0.125$, $C=-0.25$ in region ξ of Fig. 1 showing contributions from the Debye terms $p=0$ through $p=4$.
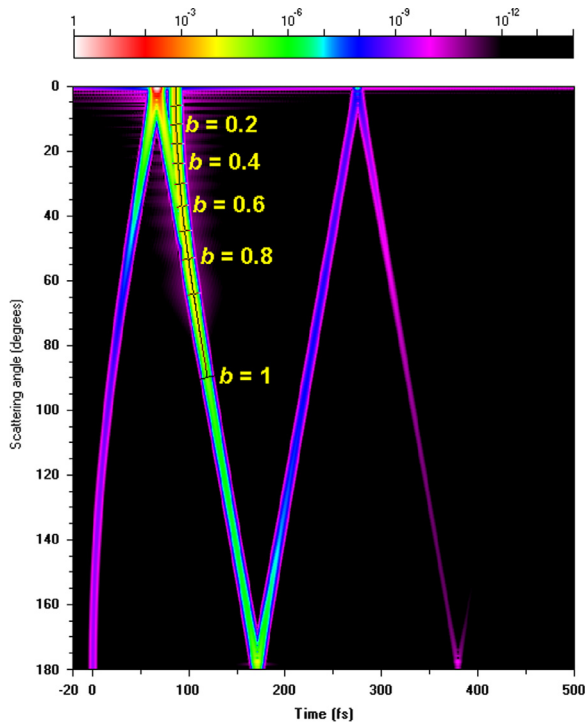
impossible for scattering of a plane wave by a homogeneous sphere because diffraction had to be combined with external reflection for partial waves n in the regime $n>2\pi a/\lambda$ in order to obtain convergence of the Mie partial wave sum. This impossibility was later verified in time domain scattering of a plane wave by a homogeneous sphere [27] because the time domain trajectory of the grazing incidence external reflection ray healed smoothly onto the smaller delay time arm of the inverted-V structure of diffraction, thus preventing a clean separation of the two processes. External reflection, however, does not occur for scattering at the surface of an edgeless Luneburg sphere. But again a separation is not possible in Fig. 8a where grazing incidence transmission of an edgeless particle-like GLL maps smoothly onto the larger delay time arm of the diffraction signature. Similarly, in Fig. 8b for an edgeless bubble-like GLL it maps smoothly onto the smaller delay time arm. In Fig. 10 for the edgeless original Luneburg lens, although small angle transmission is separated in the time domain from small angle diffraction, diffraction at larger angles maps smoothly onto transmission, again preventing the full separation.

Fig. 11, however, shows time domain scattering of an edgeless particle-like GLL with $B=2$, $C=3$ on line segment β in Fig. 1. The longer delay time arm of the inverted-V structure of diffraction is given by

$$\Delta t = a(2+\Theta)/c, \tag{14}$$

which for $a=20\,\mu m$ gives $\Delta t=133$ fs when $\Theta=0°$ and grows linearly due to large angle diffraction [15] to $\Delta t=342$ fs when $\Theta=180°$. On the other hand, Eqs. (9)–(11) of [1] show

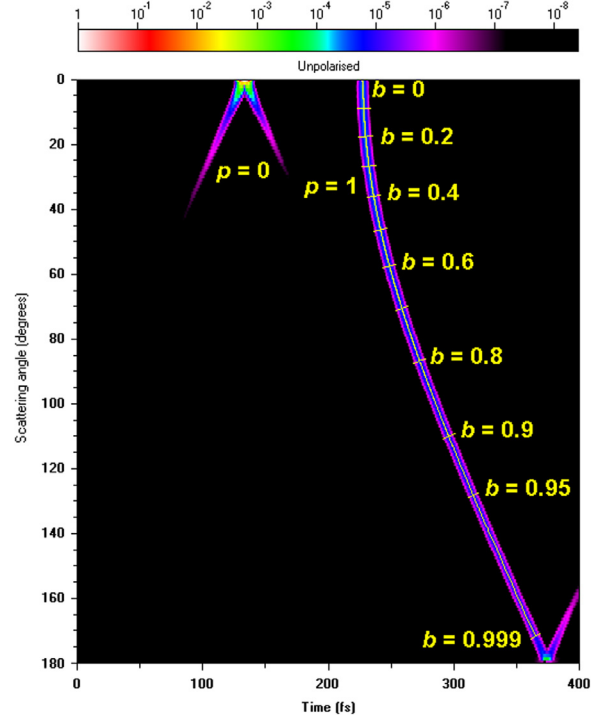**Fig. 10.** Time domain diagram for GLL of radius $a=10\,\mu m$ with $B=1$ and $C=1$ at point α in Fig. 1.

Fig. 11. Time domain diagram for a GLL of radius $a=20\,\mu m$ with $B=2$, $C=3$ on line segment β of Fig. 1 showing complete separation between the Debye $p=0$ and $p=1$ terms.

that transmission begins at $\Delta t = 228$ fs when $\Theta = 0°$ and grows to $\Delta t = 375$ fs when $\Theta = 180°$. The orbiting nature of diffraction [15] continues that physical process to yet larger scattering angles, while electromagnetic surface waves similarly continue the transmission process [9]. As a result these two time domain trajectories continue parallel to each other for large Δt, and when confined to the scattering angle interval $0° \leq \Theta \leq 180°$ occasionally cross each other with slopes of opposite sign. Fig. 11 clearly shows that diffraction has been completely separated from all other scattering processes in the time domain for this physical system.

However, as is the case for all materials, the refractive index of a real Luneburg sphere will depend on wavelength. This effect will both broaden and shift the transmission trajectory of Fig. 11 in the time domain. The broadening will be most important for a relatively short pulse containing a wide spectrum of wavelengths. One may ask whether the time domain diffraction signature in Fig. 11 will still be separated from the dispersion-broadened transmission signature when these effects are accounted for. In order to address this question, since our 5 fs full-width Gaussian pulse has a central wavelength of $\lambda_0 = 0.65$ μm, the power spectrum $1/e^2$ points correspond to $\lambda_- = 0.509$ μm and $\lambda_+ = 0.898$ μm. Since an optical frequency Luneburg sphere has yet to be fabricated, we are forced to guess at a possible wavelength dependence for $N(r, \lambda)$ with the constraint that $N(a, \lambda) = 1$ for all wavelengths to ensure that the GLL remains edgeless. We fit the real part of the refractive index of water [30] and borosilicate crown glass [31] in the visible region by the Cauchy formula, and averaged the dispersion coefficients for the two cases to get an order of magnitude estimate for a hypothetical $N(0, \lambda)$. We then parameterized $N(r, \lambda)$ by

$$N(r, \lambda) = \left[2B' - C' \left(r/a \right)^2 \right]^{1/2} \tag{15}$$

as in Eq. (1) with the Cauchy fit of B' being

$$B' = B(0.991789 + 0.035/\lambda^2 - 0.000013/\lambda^4)^2, \tag{16}$$

which gives the dispersion of $N(0, \lambda)$ being intermediate between that of water and glass, and

$$C' = 2B' - 1 \tag{17}$$

in order to guarantee that $N(a, \lambda) = 1$ for all wavelengths. Using $B = 2$, and the wavelength interval $\lambda_- \leq \lambda \leq \lambda_+$ we found that the transmission signature in Fig. 11 is widened by only about 1.7 fs, preserving the separation between the diffraction and transmission signals. We also investigated a second parameterization of dispersion that is not constrained by $N(a, \lambda) = 1$. The broadening of the transmission signal was found to be virtually identical to that of Eqs. (15–17). In addition, the group velocity of the pulse is

$$v_g = (c/n) \left[1 + (\lambda_0/n_0) \left(\mathrm{d}n/\mathrm{d}\lambda \right) \right], \tag{18}$$

which differs from c/n by only 1% and 2% for the dispersion of water and glass, respectively. This produces a corresponding small shift in the time-domain trajectory, thus claiming the imaginary prize offered in [29]. It should be noted that the fact that the broadening of the transmission signature turns out to be small provides a justification of

our hypothetical numerical estimate of dispersion in Eq. (16). This amount of broadening is applicable to the time domain plots of Figs. 8–10 as well.

5. Outlook

Although both in this paper and in [1] we limited ourselves to scattering by a generalized Luneburg lens, we believe the scattering phenomena we have uncovered here should be characteristic of the phenomena that occur for a large variety of radially inhomogeneous spheres with a generically similar refractive index profile. Although we limited ourselves to $p = 1$ transmission scattering in the context of ray theory in [1], we also believe the large variety of bow occurrences we uncovered, and which were confirmed via wave scattering and time domain scattering in this paper, should again be characteristic of their occurrences for $p \geq 2$. For example, since the ray path inside a Luneburg sphere between interactions with the surface is always a segment of an ellipse or a hyperbola one can expect that there could easily be three or more bows in a given p-channel for $p \geq 2$.

On line segments γ, δ and in portions of regions ν, ψ of Fig. 1 where only a single $p = 1$ bow occurs, the overall caustic structure organizing the bow is the morphology of the fold caustic of catastrophe theory [32,33], where the single control variable is the scattering angle Θ_1. This means that by changing the value of Θ_1 one can change the number of rays contributing to the scattered intensity from zero to two, or from two to zero. This is pictorially illustrated in Fig. 12a which is based on Fig. 3a of [32] adapted to the Luneburg geometry. The parameter B of the GLL refractive index (along with the parameter C with $C = 2B - 1$ on line segments γ, δ) is not an independent
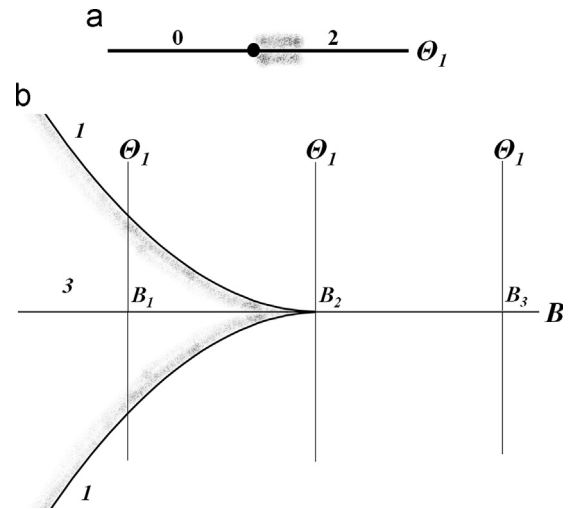

Fig. 12. (a) Fold caustic (large dot) and the scattering angle Θ_1 axis. The number of participating rays for each scattering angle is listed, and the shaded region indicates the supernumerary interference pattern. (b) Cusp caustic and the Θ_1 and B axes. The number of participating rays for each scattering angle is listed, and the shaded region indicates the supernumerary interference pattern. When $B = B_1$, two bows occur at different values of Θ_1. When $B = B_2$, the two bows coalesce at a single value of Θ_1. When $B = B_3$, no bows occur.

control variable since it does not change the overall caustic structure of two contributing rays changing to zero rays, or zero rays changing to two rays. It merely varies the scattering angle of the bow according to $\theta_i^R = \arcsin(B)$ and $\Theta_1^R = \arcsin(\pm |C|)$ if $C > 0$ or $C < 0$. The bow of line segment γ for an edgeless particle-like GLL plus that of line segment δ for an edgeless bubble-like GLL span the full extent of the single organizing fold caustic. For $0 < B < 0.5$ on line segment δ, the bow occurs at $0° \le \theta_i^R \le 45°$ and $-90° \le \Theta_1^R \le 0°$, and along line segment γ, it occurs at $45° \le \theta_i^R \le 90°$ and $0° \le \Theta_1^R \le 90°$. The $\Theta_1^R = 0°$ center point occurs when $B = 0.5$, $C = 0$, for which the sphere is absent and no scattering occurs. The $\Theta_1^R = 90°$ limit of point α in Fig. 1 evolves into the weak caustic plus the orbiting ray of the original Luneburg lens, which is shown in the ray tracing graph of Fig. 1a of [6], the wave scattering graph of Fig. 5, and the time domain scattering graph of Fig. 9. Similarly, the $\Theta_1^R = -90°$ limit of point ε evolves into the singular ray trajectory shown in Fig. 6 of [1], and the wave theory weak caustic graph of Fig. 6.

In regions η, ξ, ν where there are either two or zero $p = 1$ bows depending on the value of B and C, the bows are organized by the morphology of the cusp caustic of catastrophe theory [32,33] where the two control variables are the scattering angle Θ_1 and either B or C. This is pictorially illustrated in Fig. 12b which is based on Fig. 3b of [32] adapted to the Luneburg geometry. Depending on the value of the second control variable, the organizing cusp caustic is intersected either twice or zero times by the Θ_1 axis, giving either the two or zero observed bows and one or three contributing rays. The intersection of the Θ_1 axis with the cusp point corresponds to the coalescence of the two $p = 1$ bows which was seen in [1] to occur in region η, for example, at $B = 0.773$ when $C = 0.5$. If the second control variable is taken as B, then C is not an additional control variable, since it only serves to vary the scattering angle of the two bows, but does not change the overall caustic structure.

By way of comparison, when the shape of the scattering particle rather than its refractive index is generalized, the bow evolves into a cross section through either a hyperbolic umbilic caustic or a symbolic umbilic caustic, classified as D_4^+ and E_6, respectively, in [34–37]. This is due to the breaking of the previous spherical symmetry of the particle. Because of this symmetry loss, rays remaining in a single plane during their passage through the particle as well as skew rays whose scattering plane changes at each interaction with the particle surface participate in these higher order caustics. A similar but more complicated symmetry breaking effect occurs for glory scattering of a spheroidal particle or bubble [38,39].

In addition to the wide variety of bow appearances, $p = 1$ scattering by a GLL provides a new perspective on a number of other semi-classical scattering phenomena. As was shown in Fig. 6, the weak caustic transition can now be seen more clearly, rather than being partially obscured by its interference with other, often larger scattering processes. As was shown in Fig. 11, diffraction can be completely separated in the time domain from all other scattering processes for a certain subset of the GLLs, and as was shown in Fig. 10, the effects of orbiting for scattering

by the original Luneburg lens become quite evident in the time domain. Morphology-dependent resonances occur not only for particle-like GLLs when the incident ray just misses striking the sphere, but also for bubble-like GLLs when the incident ray is just past the critical angle for total external reflection. In both cases the resonant ray path is an ellipse lying entirely within the GLL. Additional work on scattering by a GLL remains, however. Specifically, the behavior of the interior wave when the refractive index changes from real to imaginary on line segment ζ and in region σ has not yet been quantitatively studied in wave theory.

In spite of all the details that are now understood concerning electromagnetic scattering by the simplest of all particles, a single sphere, it is exciting to see that when the refractive index profile is generalized from $C = 0$ for a homogeneous particle or bubble to $C \ne 0$ for a GLL, a large number of novel and surprising phenomena occur. The extent to which this symmetry breaking adds additional richness to $p = 1$ scattering has been seen here to be quite impressive. This richness is the hallmark of an important and deeply significant physical system that merits continuing study.

References

[1] Lock JA, Laven P, Adam JA. Scattering of a plane electromagnetic wave by a generalized Luneburg sphere. Part 1: ray scattering. J Quant Spectrosc Radiat Transf 2015 (submitted as JQSRT-D-14-00364).

[2] Debye P. Das elektromagnetische feld um einen zylinder und die theorie des regenbogens. Phys Zeit 1908;9:775–8. Translated into English in Marston PL ed. Selected Papers on Geometrical Aspects of Scattering, SPIE Milestone Series MS89. SPIE, Bellingham, WA;1994. p. 198–204.

[3] Lock JA. Scattering of an electromagnetic plane wave by a Luneburg lens. III. Finely stratified sphere model. J Opt Soc Am A 2008;25: 2991–3000.

[4] Lock JA. Debye series analysis of scattering of a plane wave by a spherical Bragg grating. Appl Opt 2005;44:5594–603.

[5] Chew WC. Waves and fields in inhomogeneous media. New York: Van Nostrand; 191–3.

[6] Lock JA. Scattering of an electromagnetic plane wave by a Luneburg lens. I. Ray theory. J Opt Soc Am A 2008;25:2971–9.

[7] Nussenzveig HM. High-frequency scattering by a transparent sphere. I. Direct reflection and transmission. J Math Phys 1969;10:82–124.

[8] Nussenzveig HM. High-frequency scattering by a transparent sphere. II. Theory of the rainbow and the glory. J Math Phys 1969;10:125–76.

[9] Lock JA, Laven P. Mie scattering in the time domain. Part I. The role of surface waves. J Opt Soc Am A 2011;28:1086–95.

[10] Fiedler-Ferrari N, Nussenzveig HM, Wiscombe WJ. Theory of near-critical-angle scattering from a curved interface. Phys Rev A 1991;43:1005–38.

[11] Marston PL. Critical angle scattering by a bubble: physical-optics approximation and observations. J Opt Soc Am 1979;69:1205–11.

[12] Marston PL, Kingsbury DL. Scattering by a bubble in water near the critical angle: interference effects. J Opt Soc Am 1981;71:192–6.

[13] Kingsbury DL, Marston PL. Mie scattering near the critical angle of bubbles in water. J Opt Soc Am 1981;71:358–61.

[14] Johnson BR. Light scattering by a multilayer sphere. Appl Opt 1996;35:3286–96.

[15] Lock JA, Laven P. Mie scattering in the time domain. Part II. The role of diffraction. J Opt Soc Am A 2011;28:1096–106.

[16] Lock JA. Scattering of an electromagnetic plane wave by a Luneburg lens. II. Wave theory. J Opt Soc Am A 2008;25:2980–90.

[17] Hill SC, Benner RE. Morphology-dependent resonances. In: Barber PW, Chang RK, editors. Optical effects associated with small particles. Singapore: World Scientific; 1988. p. 3–61.

[18] Born M, Wolf E. Principles of optics. Cambridge UK: Cambridge University Press; 121–4.

[19] Lam CC, Leung PT, Young K. Explicit asymptotic formulas for the positions, widths, and strengths of resonances in Mie scattering. J Opt Soc Am B 1992;9:1585–92.
[20] Hecht E. Optics. 2nd ed.Reading, MA: Addison-Wesley; 107–8.
[21] Johnson BR. Theory of morphology-dependent resonances: shape resonances and width formulas. J Opt Soc Am A 1993;10:343–52.
[22] van de Hulst HC. Light scattering by small particles. New York: Dover; 208–9.
[23] Marion JB, Thornton ST. Classical dynamics of particles and systems. 3rd ed.San Diego, CA: Harcourt Brace Jovanovich; 253–6.
[24] Griffiths DJ. Introduction to quantum mechanics. 2nd ed.Upper Saddle River, NJ: Pearson Prentice-Hall; 40–59.
[25] Griffiths DJ. Introduction to quantum mechanics. 2nd ed.Upper Saddle River, NJ: Pearson Prentice-Hall; 255–6.
[26] van de Hulst HC. Light scattering by small particles.New York: Dover; 203–5.
[27] Laven P. Separating diffraction from scattering: the million dollar challenge. J Nanophotonics 2010;4:041593.
[28] Laven P, 〈www.philiplaven.com/p8h2.html〉.
[29] Bohren CF, Clothiaux EE. Fundamentals of atmospheric radiation. Weinheim: Wiley-VCH; 2006. p. 126.
[30] Hale GM, Querry MR. Optical constants of water in the 200-nm to 200-µm wavelength region. Appl Opt 1973;12:555–63.
[31] Jenkins FA, White HE. Fundamentals of optics.New York: McGraw-Hill; 1950. p. 463.
[32] Berry MV. Waves and Thom's theorem. Adv Phys 1976;25:1–26.
[33] Berry MV, Upstill C. Catastrophe optics: morphologies of caustics and their diffraction patterns. Prog Opt 1980;18:257–346.
[34] Marston PL, Trinh EH. Hyperbolic umbilic diffraction catastrophe and rainbow scattering from spheroidal drops. Nature 1984;312:529–31.
[35] Nye JF. Rainbow scattering from spheroidal drops – an explanation of the hyperbolic umbilic foci. Nature 1984;312:531–2.
[36] Nye JF. Rainbows from ellipsoidal drops. Proc R Soc Lond A 1992;438:397–417.
[37] Lock JA, Xu F. Optical caustics observed in light scattered by an oblate spheroid. Appl Opt 2010;49:1288–304.
[38] Arnott WP, Marston PL. Unfolding axial caustics of glory scattering with harmonic angular perturbations of toroidal wavefronts. J Acoust Soc Am 1989;85:1427–40.
[39] Arnott WP, Marston PL. Unfolded optical glory of spheroids: back-scattering of laser light from freely rising spheroidal air bubbles in water. Appl Opt 1991;30:3429–42.